MATERIALS SCIENCE

A general printing approach for scalable growth of perovskite single-crystal films

Zhenkun Gu[1,2], Zhandong Huang[1,2], Chang Li[1,2], Mingzhu Li[1]*, Yanlin Song[1]*

Perovskite single-crystal films, which exhibit exceptionally low trap density and nearly perfect translational symmetry, are believed to achieve the highest performance of perovskite-based optoelectronic devices. However, fabrication of these perovskite single-crystal films is quite difficult because of the uncontrollable nucleation caused by the rapid reaction of two perovskite precursors. We report a facile seed printing approach to selectively create millimeter-sized perovskite single-crystal films with controlled thickness and high yield. We show that perovskite single-crystal films can be perfectly transferred to almost arbitrary substrates through the printing process. The as-grown perovskite single-crystal films have excellent crystalline quality and morphology. We further demonstrate that perovskite single-crystal films can be directly printed for scalable fabrication of photodetectors and effective image sensors. This strategy allows high-yield fabrication of large perovskite single-crystal films for functional devices and may extend to other solution-processed materials for wide applications.

INTRODUCTION

Solution-processed hybrid perovskites have been widely investigated in solar cells (*1*, *2*), light-emitting diodes (LEDs) (*3*–*6*), transistors (*7*–*9*), photodetectors (*10*), and lasers (*11*) because of their superior optoelectronic properties, such as high absorption coefficients, tunable optical properties, and long-ranged balanced electron and hole transport (*12*–*14*). Perovskite solar cells have reached a 22.1% power conversion efficiency since they were first reported in 2009 (*15*, *16*). Perovskite photodetectors have achieved high detectivity of light (*10*) and x-ray (*17*). Unfortunately, the perovskite films produced so far are typically polycrystalline (*18*–*20*) because of the uncontrollable nucleation of the deposited materials, consisting of many small grains separated by grain boundaries. Reports have demonstrated that a large density of traps exists at the grain boundaries and surfaces of perovskite polycrystalline films (*21*, *22*), which is expected to be the main reason for the obstruction of the ultimate performance of perovskite devices (*23*). Growing perovskite single-crystal films is a promising way to overcome this obstacle. However, to date, most attention has been paid to the spatial confinement method with the pressure to break the crystal isotropous growth for perovskite single-crystal films (*24*–*27*). Few works focus on the nucleation process for the film formation. The wide variation in film size, thickness, and film quality under similar growth conditions from laboratory to laboratory suggests that crucial nucleation and film growth parameters still remain uncontrolled. The ability to manipulate the nucleation and growth is important to controllably and repetitively achieve perovskite single-crystal films. However, unlike the traditional small organic molecules (*28*, *29*) and inorganic materials (*30*, *31*), hybrid perovskites create difficulty in controlling the nucleation for the film formation due to the rapid reaction of the two precursors (*18*, *32*, *33*). The uncontrollable nucleation, including random nucleation and random induced nucleation, makes the perovskite single-crystal film formation uncertain. For example, the uncontrollable nucleation density will result in polycrystalline films or stochastic pieces of single-crystal films, and the unstable nucleus size is of disadvantage to the control of film thickness. This remains a critical challenge to perovskite single-crystal film preparation. To this end, a radically controllable crystallization strategy to repetitively fabricate perovskite single-crystal films will allow scalable fabrication of high-performance perovskite devices.

Here, we report a seed-printing strategy for scalable growth of perovskite single-crystal films with controlled thickness and high yield. The key is to introduce a perovskite seed stamp into the liquid membrane system, which can significantly inhibit the random nucleation (an ultralow random nucleation density of less than 11 nuclei/cm^2) and enable the realization of accurate control of crystal growth. With this method, millimeter-sized perovskite single-crystal films were controllably prepared in batches, and the film thickness could be flexibly tailored in a wide range by the seed size. Moreover, because of the perovskite seed stamp, the perovskite single-crystal films can be perfectly transferred to almost arbitrary substrates including two-dimensional (2D) functional materials such as graphene and molybdenum disulfide (MoS_2) for exploring novel devices. Optical and electronic transport studies demonstrated that the as-grown perovskite single-crystal films exhibit high crystalline quality comparable with the best bulk perovskite single crystals reported to date. The perovskite single-crystal films were directly printed for high-yield fabrication of photodetectors, which have an ultralow dark current of 1.7 nA and a large responsivity of ~40 A/W. Furthermore, the perovskite single-crystal film was printed on high–optical-quality quartz glass to fabricate an effective image sensor. This printable strategy allows controlled growth of large perovskite single-crystal films on various substrates with high yield and enables the scalable fabrication of diverse perovskite devices.

RESULTS

Single-crystal film growth and structure characterization

To control and scale the production process of perovskite single-crystal films, we fabricated perovskite seeds on a substrate using an inkjet printing method (see Materials and Methods). Inkjet printing is a facile technology that can achieve the selective deposition of functional materials and their patterns (*34*, *35*). On this basis, perovskite solution droplets were selectively deposited onto a substrate. As the droplets evaporated, patterned perovskite seeds formed on the substrate, namely, the perovskite seed stamp, which was then covered on a target substrate with the saturated perovskite solution. With the solvent room temperature drying, single-crystal films grew in situ on the seeds uniformly across

[1]Key Laboratory of Green Printing, Institute of Chemistry, Chinese Academy of Sciences, Beijing Engineering Research Center of Nanomaterials for Green Printing Technology, Beijing National Laboratory for Molecular Sciences, Beijing 100190, P. R. China. [2]University of Chinese Academy of Sciences, Beijing 100049, P. R. China.
*Corresponding author. Email: mingzhu@iccas.ac.cn (M.L.); ylsong@iccas.ac.cn (Y.S.)

the whole substrate. Taking away the covered stamp, we directly printed the perovskite single-crystal films on the substrate (Fig. 1A). The seeds have a decisive effect on the single-crystal film formation, because they can effectively inhibit the random nucleation and trigger the growth of single-crystal films. Using this method, we controllably prepared millimeter-sized perovskite single-crystal films (for example, $CH_3NH_3PbBr_3$) in batches (Fig. 1A). The quantity and dimensions of the perovskite single-crystal films can be controlled by the number and size of the prepared seeds. To confirm the detailed morphology of the as-grown perovskite single-crystal films, we performed scanning electron microscopy (SEM) and atomic force microscopy (AFM). SEM images (fig. S1) show that the perovskite single-crystal films have a regular profile and smooth surface. AFM images (Fig. 1D and fig. S2) further ascertain the extremely smooth surface of perovskite single-crystal films with a root mean square roughness of 1.1 nm in the 30 μm × 30 μm area, which is one order of magnitude smoother than the polycrystalline films (*2*). To determine the single-crystal structure and phase purity of the films, we used synchrotron-radiated single-crystal x-ray diffraction (XRD) with a 2D detector and powder XRD. The observation of Bragg reflections (Fig. 1B and fig. S3) provides unambiguous evidence that the perovskite films are single crystalline with a long-range translational symmetry. The set of narrow peaks at (100), (200), and (300) (Fig. 1C) indicates the room temperature cubic structure and high crystal quality of the as-grown perovskite single-crystal films (*14*). The printing approach to fabricate single-crystal films can be extended to other perovskites. We prepared $CsPbBr_3$, $MAPbCl_3$, $MAPbI_3$, $(BA)_2PbBr_4$, and $(BA)_2(MA)_3Pb_4Br_{13}$ [$MA^+ = CH_3NH_3^+$, $BA^+ = CH_3(CH_2)_3NH_3^+$] single-crystal films using this seed printing method (figs. S4 and S5). The results indicate that this method can be used as a general approach to fabricate perovskite single-crystal films with high yield.

Crystallization model for perovskite single-crystal film growth

We suggest that the controllable growth of the perovskite single-crystal films by seed printing at room temperature reflects the dominant role of the introduced perovskite seeds, which can effectively suppress the random nucleation by influencing the mass transport and changing the distribution of perovskite precursor ions in the crystallization system. This has essential advantages over other temperature-induced nucleation methods for the growth of perovskite single-crystal films (*25*–*27*), which make the perovskite single-crystal film formation uncertain.

In the surface growth model, the growth process of thin films is described by the DDA (deposition, diffusion, and aggregation) model (*36*), which demonstrates a typical diffusion-controlled length scale: $l_d \approx (\frac{D}{F})^{1/6}$, where l_d is the distance of the region where no deposition occurs, D is a diffusion constant, and F is a flux of monomer. In our crystallization system, because of the existence of perovskite seeds, the crystal growth rate on the seeds is faster than in the blank area. As soon as the seeds begin to grow, mass transport to the seeds leads to the depletion of the methylammonium, lead, and bromine ions over the blank regions to the undersaturation point. Consequently, random nucleation is inhibited. To confirm this mechanism, we investigated the perovskite seed crystallization system (Fig. 2A). The experimental conditions were as follows: seed array, 10 × 10; seed distances, l = 0.1 to 2 mm; crystallization time, 30 min. The suppression ability of random nucleation is defined as N_0/N, where N_0 is the number of the origin seeds (N_0 = 100) and N is the total number of crystals within the seed regions after a

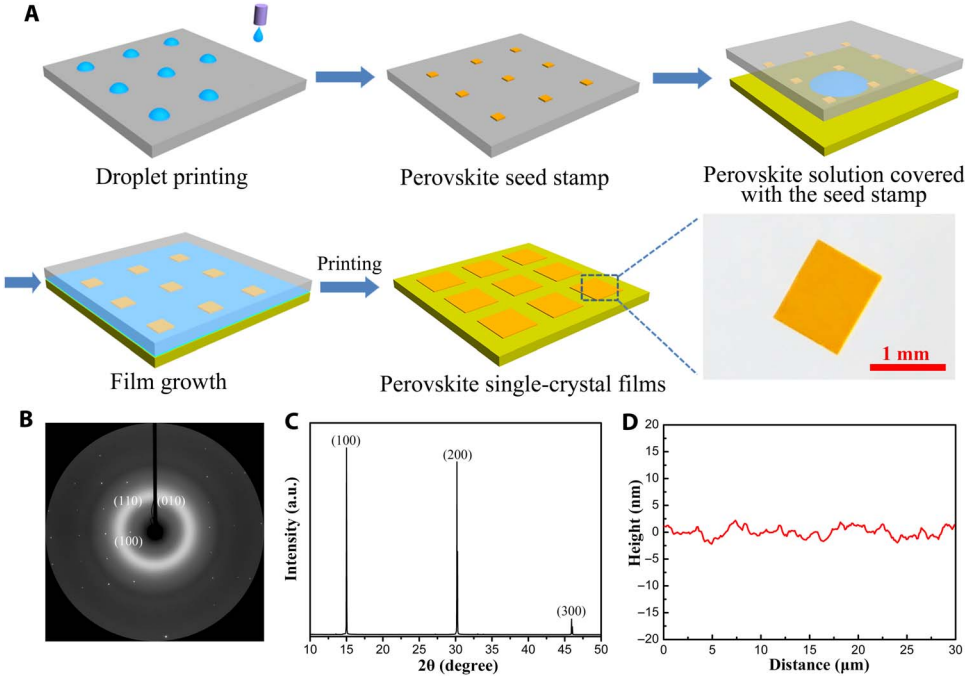

Fig. 1. Seed printing of perovskite single-crystal films. (**A**) Schematic illustration of the scalable growth of perovskite single-crystal films. First, perovskite seed stamp is fabricated using an inkjet printing method. Second, the prepared seed stamp is covered on the target substrate with perovskite solution, and perovskite single-crystal films in situ grow as the solvent dries. Taking away the covered stamp, we printed the perovskite single-crystal films on the substrate. Scale bar, 1 mm. (**B**) Synchrotron-radiated single-crystal XRD photograph of the perovskite film on quartz glass by rotating the incident x-ray angle of ±22.5°. All the diffraction rings belonged to the quartz glass substrate. (**C**) XRD pattern for the perovskite single-crystal film. a.u., arbitrary units. (**D**) AFM profile of the perovskite single-crystal film surface.

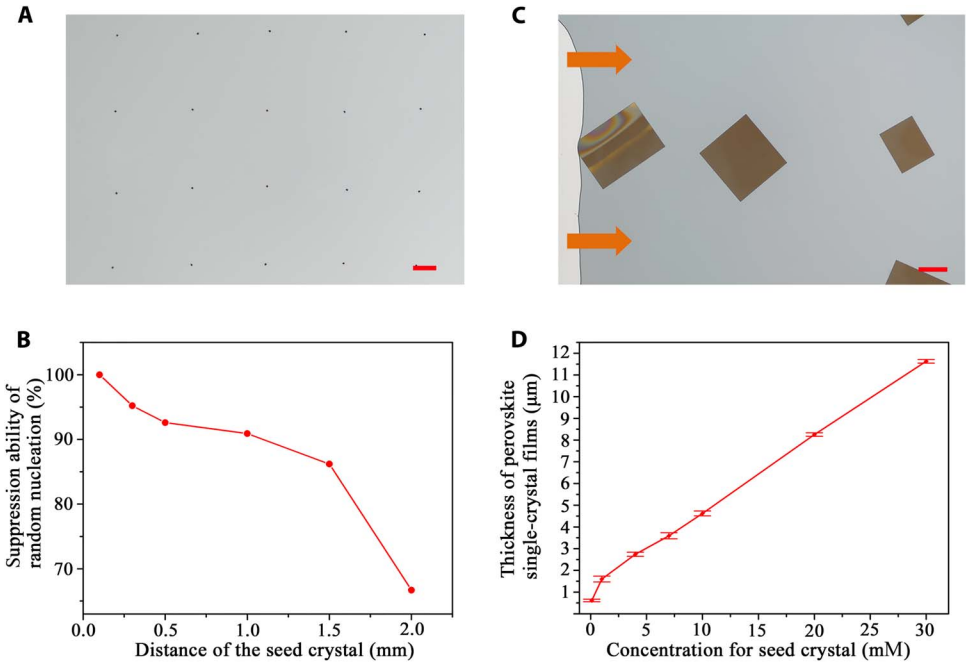

Fig. 2. The inhibition of random nucleation and film growth. (**A**) Optical image of the patterned perovskite seeds for the growth of perovskite single-crystal films. Scale bar, 100 μm. (**B**) Suppression ability of random nucleation as a function of the distance of seeds. The suppression ability of random nucleation was defined as N_0/N, where N_0 is the number of the origin perovskite seeds (N_0 = 100) and N is the total number of crystals within the seed regions after a crystallization time of 30 min. (**C**) Photo of perovskite seeds with the distance l = 0.5 mm growing on quartz glass for 24 hours. It can be observed that the outside films are larger than the inside ones, and no excrescent nucleation exists between the seeds. Scale bar, 100 μm. (**D**) Thickness of perovskite single-crystal films on quartz glass as a function of the seed size, which is controlled by the concentration of printed perovskite solution. It shows that the perovskite single-crystal film thickness approximately linearly increases with the seed size and that the thickness of the perovskite single-crystal films can be flexibly tuned by the origin seed size from hundreds of nanometers to more than ten micrometers.

certain crystallization time. It was observed that the introduced seeds can suppress random nucleation (Fig. 2B). When the seed distance l is less than 1 mm, the suppression ability of random nucleation can be greater than 90% (an ultralow random nucleation density of less than 11 nuclei/cm^2), and the growth of the perovskite single-crystal film was only observed in the seed region (hardly any nucleation occurred within ~1.0 mm of the active area) (fig. S6). In this case, perovskite single-crystal films were controllably prepared in batches (fig. S7). The perovskite single-crystal film growth process was monitored, and it was found that the growth of perovskite single-crystal films actually underwent a two-step growth process (fig. S8). When the perovskite seeds contacted the liquid membrane, the rapid depletion of the methylammonium, lead, and bromine ions over the blank regions led to fast growth of perovskite single-crystal films (first 30 min). As the solvent gradually evaporated from the open side of the liquid membrane, the increment of solution concentration enabled the secondary slow growth of perovskite single-crystal films. This two-step growth mechanism was believed to be the key to the formation of high-quality single-crystal films: The fast growth process, which rapidly depleted the saturated ions, would inhibit the random nucleation in the early stage of the crystallization, and the slow growth process ensured the high quality of the film. Indeed, perovskite single-crystal film growth in this method presents high crystal quality (discussed in detail in Fig. 3). As an example, Fig. 2C shows the seed pattern growing on quartz glass for 24 hours. It is obviously found that the outside films are larger than the inside ones and that no excrescent nucleation exists between the single-crystal films, which also proves the two-step growth process with the retraction of the liquid membrane.

Different perovskite film thicknesses can meet the requirement of various optoelectronic devices, and at the same time, the proper thickness is recognized as a key parameter to the device performance. Here, the introduced perovskite seeds can not only inhibit the random nucleation but also flexibly tailor perovskite single-crystal film thickness. The thickness relationship between the seed size and perovskite single-crystal film is shown in Fig. 2D (details in fig. S9). It shows that the thickness of the perovskite single-crystal film increases with the origin seed size, which can be well controlled by the concentration of printed perovskite solution. By tailoring the seed size, we can approximately linearly control the perovskite single-crystal film thickness from hundreds of nanometers to more than ten micrometers. These results will extend perovskite single-crystal films for exploring high-performance devices and various applications.

Optical and trap density property

The absorbance of perovskite single-crystal films (Fig. 3A) presents a clear absorption cutoff at 535 nm with no excitonic signature, and film interference after 550 nm is observed, which indicates a minimal trap density and high flatness of the perovskite single-crystal films. The narrow photoluminescence (PL) peak near the bandgap also manifests a lower trap density in the perovskite single-crystal films (Fig. 3A). A fluorescence microscopy image of perovskite single-crystal films is shown in Fig. 3B, and the uniform bright luminescence of the film shows high quality with no visible defects.

The trap density of the as-grown perovskite single-crystal films was estimated using the space charge–limited current technique (*26*). As

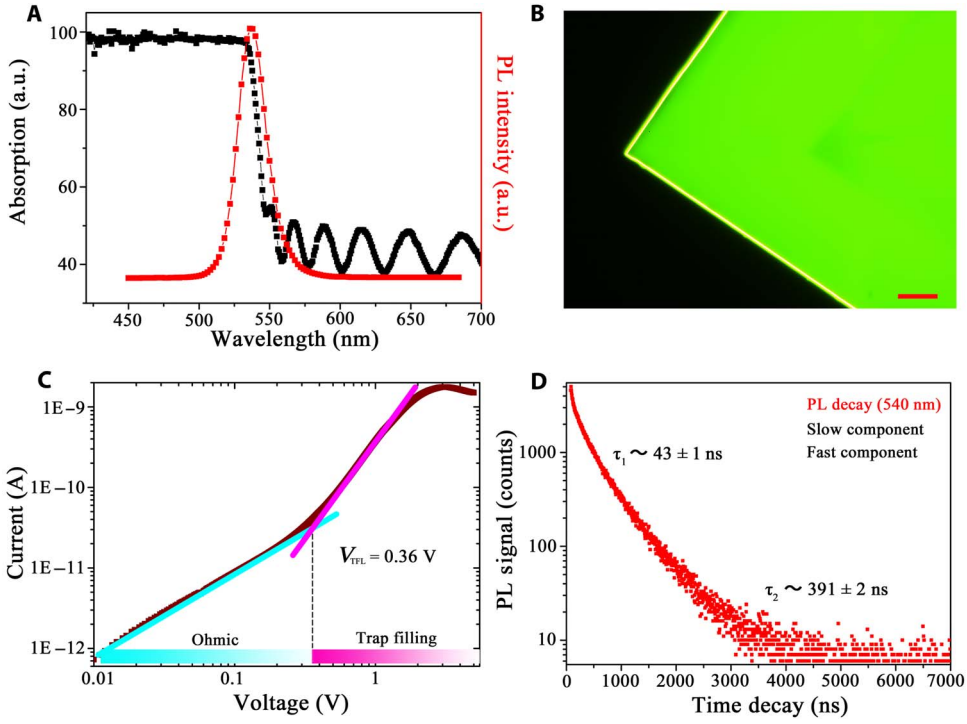

Fig. 3. Optical and trap density property. (**A**) Steady-state micro-area absorbance and PL of the perovskite single-crystal films. PL excitation wavelength is 405 nm. (**B**) Fluorescence microscopy image of the perovskite single-crystal film. The uniform luminescence of the film verifies its high quality without visible defects. Scale bar, 50 μm. (**C**) Current-voltage trace of perovskite single-crystal films. It shows a linear ohmic region followed by the trap-filled region at V_{TFL} = 0.36 V. The trap density determined by V_{TFL} was calculated as $n_{trap} = 2.6 \times 10^{-10}$ cm^{-3}. (**D**) PL time decay trace of the perovskite single-crystal films at 540 nm showing a fast component (τ_1 = 43 ns) and a slow component (τ_2 = 391 ns).

shown in Fig. 3C, at low bias, the *I-V* traces presented an ohmic response, as confirmed by the linear fit of the *I-V* relation. At high bias, the traps were markedly filled with the rapid nonlinear rise of the current, which suggested the trap-filled limit (TFL) regime. The trap density determined by V_{TFL} was calculated as 2.6×10^{-10} cm^{-3}, which is comparable with the best bulk perovskite single crystals reported to date (*13*, *14*). To investigate the exciton lifetime of the perovskite single-crystal films, we monitored the PL decay of the perovskite single-crystal films using the transient steady-state spectrometer. The PL time decay trace strictly fitted to the biexponential mode. Two dynamics, including a fast component of τ = 43 ns together with a longer-lived decay of τ = 391 ns, were observed in the perovskite single-crystal films (Fig. 3D), which can be assigned to the surface and bulk recombination (*14*). All these results above suggested the high quality of the as-grown perovskite single-crystal films.

Printing perovskite single-crystal films on various substrates

Optoelectronic applications require not only high-quality perovskite single-crystal films but also their controllable growth on various substrates. For the traditional materials, such as graphene and MoS_2, the transfer approaches are mostly based on the complete etching methods. It leads to inevitable damage to the original films and increases the production cost (*37*, *38*). The perovskite seed stamp we used here allows the direct printing of perovskite single-crystal films on various substrates nondestructively during the growth process (Fig. 4), including glass, quartz glass, silicon wafer, fluorine-doped tin oxide (FTO) glass, polyethylene terephthalate (PET) film, polyethylene (PE) film, and polyimide (PI) film. What is more, perovskite single-crystal films can directly grow on graphene and MoS_2 to form heterostructures for exploring novel devices.

Scalable fabrication of photodetectors

The seed printing method allows facile production of high-quality perovskite single-crystal films with high yield. Using this method, we directly printed perovskite single-crystal films for scalable fabrication of photodetectors. The device structure used is depicted in Fig. 5A. The dark *I-V* trace of the device (Fig. 5B) shows an ultralow dark current of 1.7 nA, which further demonstrates the low trap density of the single-crystal films and predicts high signal-to-noise ratio of the photodetector. The transient photocurrent of the photodetector exhibits good on/off photoswitching behavior (Fig. 5D). The responsivity increases with the decrease of incident light intensity in a weak light range, and a large responsivity up to ~40 A/W (at 54 μW/cm^2) was measured under a 450-nm monochromatic source (Fig. 5C and fig. S10). The results show that this method allows high-yield fabrication of perovskite functional devices.

Image sensor based on the perovskite single-crystal film

As this method can directly print high-quality perovskite single-crystal films on different substrates, we further printed the perovskite single-crystal film on a high–optical quality quartz glass and fabricated an effective image sensor to demonstrate its usefulness. An array of Au electrodes with a thickness of 120 nm was deposited on the perovskite single-crystal film (Fig. 6A). We investigated different region photoresponses of individual perovskite single-crystal films. The photocurrent mapping (180 μm × 180 μm) of the perovskite single-crystal film

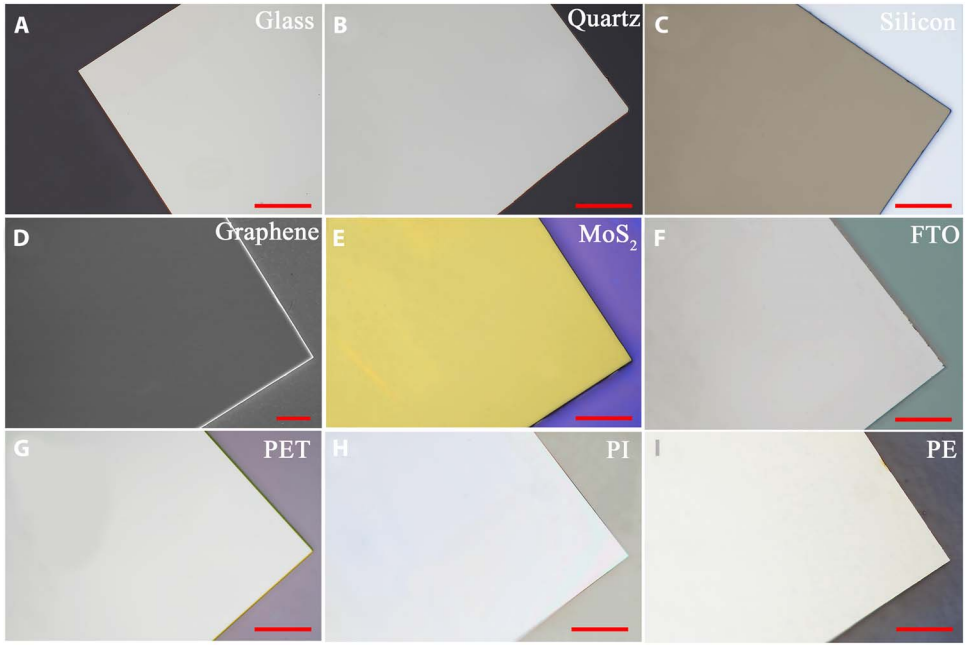

Fig. 4. Printing perovskite single-crystal film on various kinds of substrates. Optical microscopy images of the perovskite single-crystal film on (**A**) glass, (**B**) quartz glass, and (**C**) silicon wafer. (**D**) SEM image of the perovskite single-crystal film on graphene. Optical microscopy images of the perovskite single-crystal film on (**E**) MoS_2, (**F**) FTO glass, (**G**) PET film, (**H**) PI film, and (**I**) PE film. Scale bars, 50 μm (A to C and E to I) and 5 μm (D).

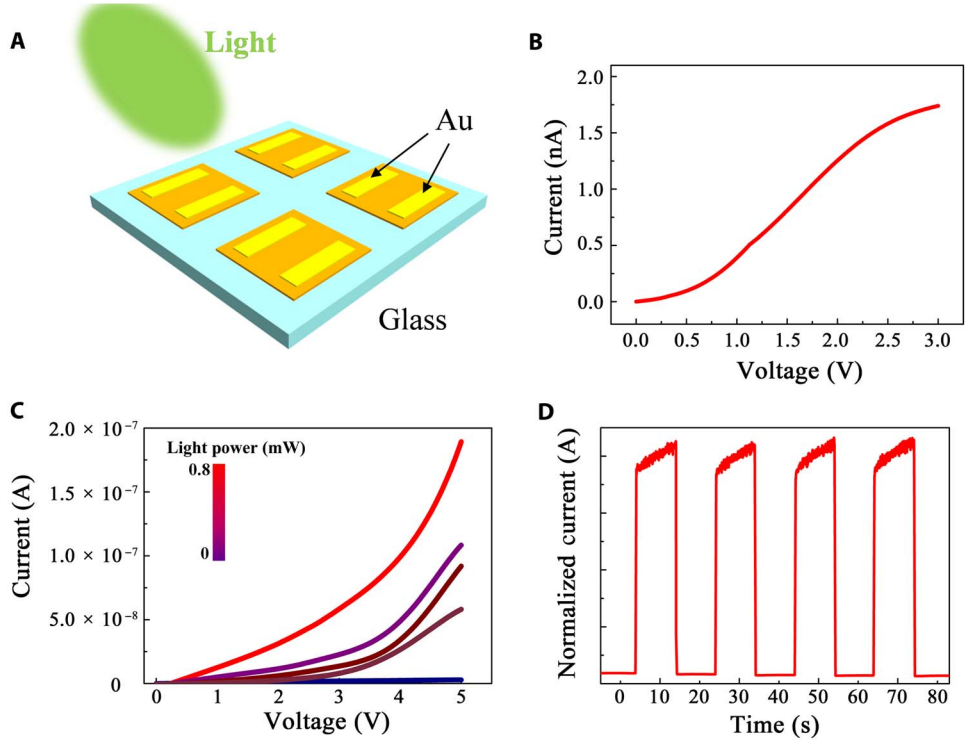

Fig. 5. Scalable fabrication of photodetectors. (**A**) Schematic device structure of the perovskite single-crystal photodetectors. (**B**) Current-voltage characteristic measured in the dark condition. (**C**) Current-voltage curve in different incident light intensities. (**D**) Transient photocurrent of the photodetector (bias, 3 V; λ = 450 nm).

(Fig. 6B) shows that all the regions under the illumination present a strong photoresponse. Compared to the reported 1D perovskite microwire array and the 2D perovskite thin film (*39*), only 2.6% photocurrent fluctuation was observed at the perovskite single-crystal film. In particular, there is no obvious photocurrent change along the horizontal and vertical directions, which reveals the high uniformity of the device. This can be attributed to the homogeneous structure of the printed single-crystal film, such as the exceptionally low trap density and lack of grain boundaries.

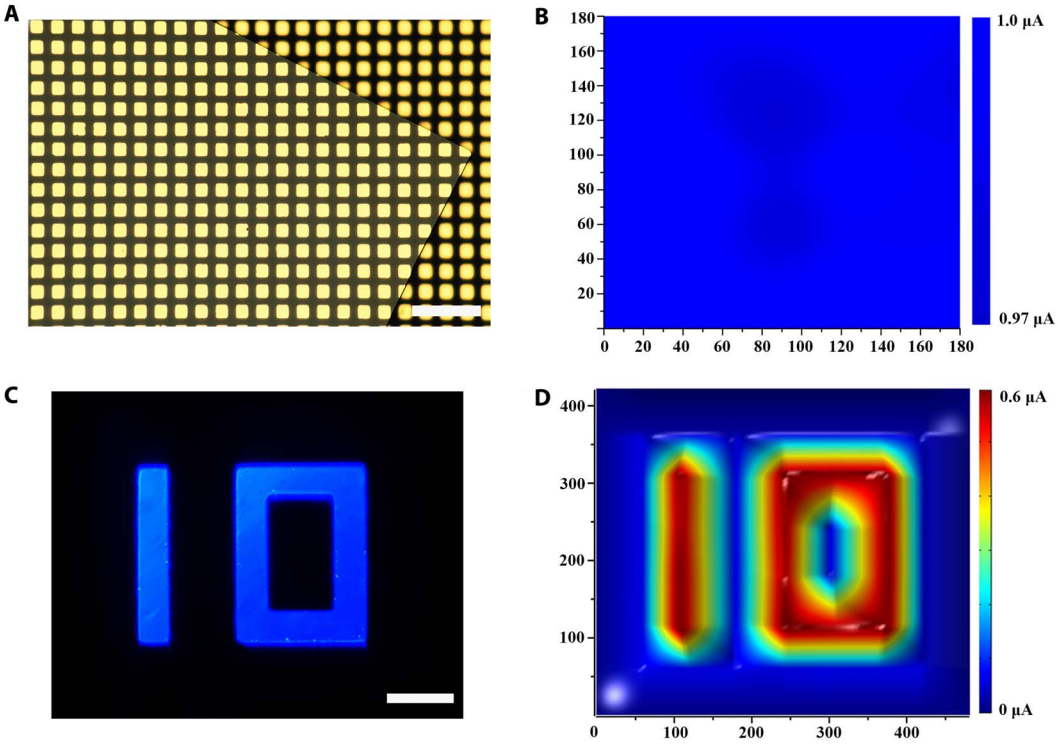

Fig. 6. Image sensor based on the perovskite single-crystal film. (**A**) Optical image of electrode arrays on the perovskite single-crystal film. Scale bar, 200 μm. (**B**) Photocurrent mapping of the perovskite single-crystal film. (**C**) Optical image of the number 10. Scale bar, 100 μm. (**D**) Photocurrent intensity profile of the optical image 10.

To this end, an optical image character "10" was illuminated from the back of electrode arrays (Fig. 6C). The photoresponse from the electrode arrays shows that all the regions exposed to the illumination present a clear and uniform photocurrent response with 100% yield (Fig. 6D). The photocurrent mapping generated by the device based on the single-crystal film shows a clear number 10 image (Fig. 6D). There is no obvious photocurrent variation on the optical image, which demonstrates that this homogeneous printed single-crystal film can be applied as an effective image sensor.

DISCUSSION

Here, we demonstrate a facile seed printing strategy for scalable growth of perovskite single-crystal films with controlled thickness and high yield. The process relies on the introduced perovskite seeds in the crystallization system, which can effectively suppress the random nucleation by influencing the mass transport and changing the distribution of perovskite precursor ions. On this basis, we show that this method can be used as a general approach to fabricate different kinds of perovskite single-crystal films, including $CsPbBr_3$, $MAPbCl_3$, $MAPbI_3$, $(BA)_2PbBr_4$, and $(BA)_2(MA)_3Pb_4Br_{13}$. The as-grown perovskite single-crystal films can be directly printed on various substrates, and the film thickness can be flexibly tailored in a wide range by the seed size. The perovskite single-crystal films show high crystalline quality compared with the best quality of bulk perovskite single crystals reported to date. We further show that the perovskite single-crystal films can be directly printed for high-yield fabrication of photodetectors. Moreover, the perovskite single-crystal film was printed on a high–optical quality quartz glass to fabricate an effective image sensor. The present results show that perovskite single-crystal films were controllably fabricated with high yield, but for practical film applications, perovskite single-crystal films with centimeter size or a larger size are also very important. Preliminary results from our laboratory suggest that this is possible using multiple growth processes. This method offers an effective way to controllably fabricate different kinds of perovskite single-crystal films with high yield and high reproducibility. It will be of great significance for the development of diverse perovskite functional devices, such as solar cells, LEDs, transistors, and laser diodes, and can also be possibly extended to other solution-processed materials for wide application.

MATERIALS AND METHODS

Materials

Cesium bromide (CsBr; 99.999%), lead chloride ($PbCl_2$; 99.999%), lead bromide ($PbBr_2$; 99.999%), and lead iodide (PbI_2; 99.999%) were purchased from Sigma-Aldrich. Methylammonium chloride (MACl; >99.5%), methylammonium bromide (MABr; >99.5%), methylammonium iodide (MAI; >99.5%), and butylammonium bromide (BABr; >99.5%) were purchased from Xi'an Polymer Light Technology Corporation. Dimethyl sulfoxide (DMSO; 99.9%), γ-butyrolactone (GBL; 99.9%), and *N*,*N*-dimethylformamide (DMF; 99.9%) were purchased from Aladdin Reagent Ltd. All these materials were used as received without further purification.

Perovskite saturated solution preparation

To prepare the perovskite saturated solution, stoichiometric quantities of the perovskite precursors were fully dissolved in DMF [for $CsPbBr_3$, $CH_3NH_3PbBr_3$, $(BA)_2PbBr_4$, and $(BA)_2(MA)_3Pb_4Br_{13}$], DMSO (for $CH_3NH_3PbCl_3$), and GBL (for $CH_3NH_3PbI_3$) to obtain a high concentration of perovskite solution. Then, the prepared solution was transferred

to a 20-ml opened bottle for evaporation at room temperature to obtain a saturated solution that contained small single crystals. The solution was filtered using a polytetrafluoroethylene filter with a 0.1-μm pore size to obtain clear perovskite saturated solution for the growth of perovskite single-crystal films.

Perovskite seed stamp preparation

The perovskite seeds were prepared using an inkjet printing method. First, diluted perovskite inks were prepared by dissolving stoichiometric quantities of perovskite precursors in DMSO (for $CsPbBr_3$, $CH_3NH_3PbBr_3$, and $CH_3NH_3PbCl_3$), DMF [for $(BA)_2PbBr_4$ and $(BA)_2(MA)_3Pb_4Br_{13}$], and GBL (for $CH_3NH_3PbI_3$). Then the perovskite inks were printed on a fluorosilane-functionalized silicon wafer using a Fujifilm Dimatix DMP-2800 printer. As the droplets evaporated, ordered perovskite seeds formed on the silicon wafer. The seed crystal size and distance can be controlled by the concentration of perovskite inks and the printer. We used the perovskite seeds together with their supporting substrate to form the perovskite seed stamp.

Substrate preparation

Silicon wafer, glass, quartz glass, FTO glass, PET, PI, and PE films were rinsed in an ultrasonic bath in alcohol and ultrapure water for 30 min each. The single-layer graphene was prepared by the chemical vapor deposition (CVD) method on the Cu substrate (*30*). The MoS_2 was prepared by the CVD method on the SiO_2/Si substrate (*38*).

Synthesis of perovskite single-crystal films

To grow perovskite single-crystal films, 0.5 μl of saturated precursor solution was dropped on the surface of the target substrate. Then, the target substrate was covered with the perovskite seed stamp (1 cm × 1 cm) and a 100-g weight. Drying the solvent completely at room temperature and the in situ growth process of single-crystal films occurred uniformly across the whole substrate.

Measurement and characterization

Optical images of perovskite single-crystal films were obtained using a Nikon LV100ND optical microscope. The SEM images were captured using a JEOL JSM-7500 field-emission SEM operated at 15 kV. The synchrotron-radiated single-crystal XRD was performed in the 15U1 beamline at Shanghai Synchrotron Radiation Facility. The x-ray beam we used has a wavelength of 0.6199 Å. The monochromated x-ray beam was focused on the perovskite film on quartz glass with a size of 3 μm × 3 μm in at least five positions. The Bragg reflections were detected using a MAR-165 charge-coupled device detector with an exposure time of 50 s. The XRD was measured using a PANalytical Empyrean x-ray powder diffractometer equipped with a 2.2-kW Cu α radiation. Energy-dispersive spectroscopy (EDS) of perovskite single-crystal films was carried out using the JEOL JSM-7500 field-emission SEM equipped with an EDS detector operated at 15 kV. The thickness of the perovskite single-crystal films was measured using a Bruker ContourGT optical profilometer in a VSI/VXI mode. The scan speed was 1× with a backscan length of 2 μm. Micro-area absorbance was measured in transmission mode with a 120-μm light spot using a Fuxiang micro-area ultraviolet-visible absorbance spectroscope. The PL spectrum was measured using an Olympus FV1000-IX81 laser scanning confocal microscope equipped with a 405-nm laser. The *I-V* traces were measured using a Micromanipulator probe station with a Keithley 4200 semiconductor measurement system at room temperature in the dark environment. Perovskite single-crystal films were directly grown on quartz glass with the patterned Au electrodes. The trap density of perovskite single-crystal films n_{trap} was calculated using the trap-filled limit voltage $V_{TFL} = en_{trap}L^2/2\varepsilon\varepsilon_0$, where e is the electronic charge, L is the channel width, ε is the dielectric constant of perovskite materials (25.5 for $MAPbBr_3$) (*13*, *14*), and ε_0 is the vacuum permittivity. PL decay measurements at 540 nm were performed using an Edinburgh FLS 980 transient steady-state spectrometer with a 405-nm laser. Perovskite single-crystal films grown on the quartz glass were chosen for the sample. For the analysis of the time-resolved traces, multi-exponential profiles were used as trial fit functions.

Photodetector fabrication and characterizations

The printed perovskite single-crystal films on quartz glass were used to fabricate the single-crystal photodetectors. Two 80-nm-thick Au films as the top electrodes were deposited on the films with a channel width of 25 μm. The effective illuminated area was 2.5×10^{-9} m^2. The responsivity R was calculated using I_{light}/P_{in}, where I_{light} is the photocurrent and P_{in} is the incident light intensity. For the responsivity measurement, a blue monochromatic 450-nm laser source was used. The *I-V* traces were measured using a Micromanipulator probe station with a Keithley 4200 semiconductor measurement system at room temperature.

Image sensor fabrication and characterizations

The perovskite single-crystal film was directly printed on the high–optical quality quartz glass to fabricate an image sensor. An array of Au electrodes with a thickness of 120 nm was deposited on the perovskite single-crystal film. A LED light of 450 nm illuminated the apparatus from the back of electrode arrays. For the image light, an optical mask with the image character 10 was pasted onto the back of the quartz glass. The *I-V* traces were measured using a Micromanipulator probe station with two 6-μm probes and Keithley 4200 semiconductor measurement system at room temperature.

SUPPLEMENTARY MATERIALS

Supplementary material for this article is available at http://advances.sciencemag.org/cgi/content/full/4/6/eaat2390/DC1

fig. S1. The SEM images of the as-grown perovskite single-crystal film.
fig. S2. Optical microscopy image and AFM image of the perovskite single-crystal film.
fig. S3. Synchrotron-radiated single-crystal XRD analysis.
fig. S4. EDS mappings of the perovskite single-crystal films.
fig. S5. Powder XRD patterns of the perovskite single-crystal films.
fig. S6. Optical microscopy images of the seed crystal regions.
fig. S7. Scalable fabrication of perovskite single-crystal films.
fig. S8. Perovskite single-crystal film growth process.
fig. S9. The height profiles of perovskite single-crystal films with different thicknesses.
fig. S10. Responsivity as a function of incident light intensity.

REFERENCES AND NOTES

1. H. Zhou, Q. Chen, G. Li, S. Luo, T.-b. Song, H.-S. Duan, Z. Hong, J. You, Y. Liu, Y. Yang, Interface engineering of highly efficient perovskite solar cells. *Science* **345**, 542–546 (2014).
2. X. Li, D. Bi, C. Yi, J.-D. Décoppet, J. Luo, S. M. Zakeeruddin, A. Hagfeldt, M. Grätzel, A vacuum flash–assisted solution process for high-efficiency large-area perovskite solar cells. *Science* **353**, 58–62 (2016).
3. H. Cho, S.-H. Jeong, M.-H. Park, Y.-H. Kim, C. Wolf, C.-L. Lee, J. H. Heo, A. Sadhanala, N. Myoung, S. Yoo, S. H. Im, R. H. Friend, T.-W. Lee, Overcoming the electroluminescence efficiency limitations of perovskite light-emitting diodes. *Science* **350**, 1222–1225 (2015).
4. Y.-H. Kim, H. Cho, J. H. Heo, T.-S. Kim, N. Myoung, C.-L. Lee, S. H. Im, T.-W. Lee, Multicolored organic/inorganic hybrid perovskite light-emitting diodes. *Adv. Mater.* **27**, 1248–1254 (2015).
5. Y.-H. Kim, H. Cho, T.-W. Lee, Metal halide perovskite light emitters. *Proc. Natl. Acad. Sci. U.S.A.* **113**, 11694–11702 (2016).
6. Z.-K. Tan, R. S. Moghaddam, M. L. Lai, P. Docampo, R. Higler, F. Deschler, M. Price, A. Sadhanala, L. M. Pazos, D. Credgington, F. Hanusch, T. Bein, H. J. Snaith, R. H. Friend,

Bright light-emitting diodes based on organometal halide perovskite. *Nat. Nanotechnol.* **9**, 687–692 (2014).
7. D. Li, H.-C. Cheng, Y. Wang, Z. Zhao, G. Wang, H. Wu, Q. He, Y. Huang, X. Duan, The effect of thermal annealing on charge transport in organolead halide perovskite microplate field-effect transistors. *Adv. Mater.* **29**, 1601959 (2017).
8. D. Li, G. Wang, H.-C. Cheng, C.-Y. Chen, H. Wu, Y. Liu, Y. Huang, X. Duan, Size-dependent phase transition in methylammonium lead iodide perovskite microplate crystals. *Nat. Commun.* **7**, 11330 (2016).
9. G. Wang, D. Li, H.-C. Cheng, Y. Li, C.-Y. Chen, A. Yin, Z. Zhao, Z. Lin, H. Wu, Q. He, M. Ding, Y. Liu, Y. Huang, X. Duan, Wafer-scale growth of large arrays of perovskite microplate crystals for functional electronics and optoelectronics. *Sci. Adv.* **1**, e1500613 (2015).
10. L. Dou, Y. M. Yang, J. You, Z. Hong, W.-H. Chang, G. Li, Y. Yang, Solution-processed hybrid perovskite photodetectors with high detectivity. *Nat. Commun.* **5**, 5404 (2014).
11. G. Xing, N. Mathews, S. S. Lim, N. Yantara, X. Liu, D. Sabba, M. Grätzel, S. Mhaisalkar, T. C. Sum, Low-temperature solution-processed wavelength-tunable perovskites for lasing. *Nat. Mater.* **13**, 476–480 (2014).
12. Q. Dong, Y. Fang, Y. Shao, P. Mulligan, J. Qiu, L. Cao, J. S. Huang. Electron-hole diffusion lengths > 175 μm solution-grown $CH_3NH_3PbI_3$ single crystals. *Science* **347**, 967–970 (2015).
13. D. Shi, V. Adinolfi, R. Comin, M. Yuan, E. Alarousu, A. Buin, Y. Chen, S. Hoogland, A. Rothenberger, K. Katsiev, Y. Losovyj, X. Zhang, P. A. Dowben, O. F. Mohammed, E. H. Sargent, O. M. Bakr, Low trap-state density and long carrier diffusion in organolead trihalide perovskite single crystals. *Science* **347**, 519–522 (2015).
14. M. I. Saidaminov, A. L. Abdelhady, B. Murali, E. Alarousu, V. M. Burlakov, W. Peng, I. Dursun, L. Wang, Y. He, G. Maculan, A. Goriely, T. Wu, O. F. Mohammed, O. M. Bakr, High-quality bulk hybrid perovskite single crystals within minutes by inverse temperature crystallization. *Nat. Commun.* **6**, 7586 (2015).
15. W. S. Yang, B.-W. Park, E. H. Jung, N. J. Jeon, Y. C. Kim, D. U. Lee, S. S. Shin, J. Seo, E. K. Kim, J. H. Noh, S. I. Seok, Iodide management in formamidinium-lead-halide–based perovskite layers for efficient solar cells. *Science* **356**, 1376–1379 (2017).
16. Z. H. Kafafi, R. J. Martín-Palma, A. F. Nogueira, D. M. O'Carroll, J. J. Pietron, I. D. W. Samuel, F. So, N. Tansu, L. Tsakalakos, The role of photonics in energy. *J. Photonics Energy* **5**, 050997 (2015).
17. S. Yakunin, M. Sytnyk, D. Kriegner, S. Shrestha, M. Richter, G. J. Matt, H. Azimi, C. J. Brabec, J. Stangl, M. V. Kovalenko, W. Heiss, Detection of x-ray photons by solution-processed lead halide perovskites. *Nat. Photonics* **9**, 444–449 (2015).
18. N. J. Jeon, J. H. Noh, Y. C. Kim, W. S. Yang, S. Ryu, S. I. Seok, Solvent engineering for high-performance inorganic-organic hybrid perovskite solar cells. *Nat. Mater.* **13**, 897–903 (2014).
19. Y. Deng, E. Peng, Y. Shao, Z. Xiao, Q. Dong, J. Huang, Scalable fabrication of efficient organolead trihalide perovskite solar cells with doctor-bladed active layers. *Energy Environ. Sci.* **8**, 1544–1550 (2015).
20. F. Ye, H. Chen, F. Xie, W. Tang, M. Yin, J. He, E. Bi, Y. Wang, X. Yang, L. Han, Soft-cover deposition of scaling-up uniform perovskite thin films for high cost-performance solar cells. *Energy Environ. Sci.* **9**, 2295–2301 (2016).
21. I. A. Shkrob, T. W. Marin, Charge trapping in photovoltaically active perovskites and related halogenoplumbate compounds. *J. Phys. Chem. Lett.* **5**, 1066–1071 (2014).
22. N. K. Noel, A. Abate, S. D. Stranks, E. S. Parrott, V. M. Burlakov, A. Goriely, H. J. Snaith, Enhanced photoluminescence and solar cell performance via Lewis base passivation of organic–inorganic lead halide perovskites. *ACS Nano* **8**, 9815–9821 (2014).
23. Y. Liu, Z. Yang, D. Cui, X. Ren, J. Sun, X. Liu, J. Zhang, Q. Wei, H. Fan, F. Yu, X. Zhang, C. Zhao, S. F. Liu, Two-inch-sized perovskite $CH_3NH_3PbX_3$ (X = Cl, Br, I) crystals: Growth and characterization. *Adv. Mater.* **27**, 5176–5183 (2015).
24. H.-S. Rao, B.-X. Chen, X.-D. Wang, D.-B. Kuang, C.-Y. Su, A micron-scale laminar $MAPbBr_3$ single crystal for an efficient and stable perovskite solar cell. *Chem. Commun.* **53**, 5163–5166 (2017).
25. Y. Liu, Y. Zhang, Z. Yang, D. Yang, X. Ren, L. Pang, S. F. Liu, Thinness- and shape-controlled growth for ultrathin single-crystalline perovskite wafers for mass production of superior photoelectronic devices. *Adv. Mater.* **28**, 9204–9209 (2016).
26. Y.-X. Chen, Q.-Q. Ge, Y. Shi, J. Liu, D.-J. Xue, J.-Y. Ma, J. Ding, H.-J. Yan, J.-S. Hu, L.-J. Wan, General space-confined on-substrate fabrication of thickness-adjustable hybrid perovskite single-crystalline thin films. *J. Am. Chem. Soc.* **138**, 16196–16199 (2016).
27. Z. Chen, Q. Dong, Y. Liu, C. Bao, Y. Fang, Y. Lin, S. Tang, Q. Wang, X. Xiao, Y. Bai, Y. Deng, J. Huang, Thin single crystal perovskite solar cells to harvest below-bandgap light absorption. *Nat. Commun.* **8**, 1890 (2017).
28. Y. Diao, B. C.-K. Tee, G. Giri, J. Xu, D. H. Kim, H. A. Becerril, R. M. Stoltenberg, T. H. Lee, G. Xue, S. C. B. Mannsfeld, Z. Bao, Solution coating of large-area organic semiconductor thin films with aligned single-crystalline domains. *Nat. Mater.* **12**, 665–671 (2013).
29. H. Minemawari, T. Yamada, H. Matsui, J. Tsutsumi, S. Haas, R. Chiba, R. Kumai, T. Hasegawa, Inkjet printing of single-crystal films. *Nature* **475**, 364–367 (2011).
30. H. Zhou, W. J. Yu, L. Liu, R. Cheng, Y. Chen, X. Huang, Y. Liu, Y. Wang, Y. Huang, X. Duan, Chemical vapour deposition growth of large single crystals of monolayer and bilayer graphene. *Nat. Commun.* **4**, 2096 (2013).
31. G. Lu, T. Wu, Q. Yuan, H. Wang, H. Wang, F. Ding, X. Xie, M. Jiang, Synthesis of large single-crystal hexagonal boron nitride grains on Cu–Ni alloy. *Nat. Commun.* **6**, 6160 (2015).
32. M. Liu, M. B. Johnston, H. J. Snaith, Efficient planar heterojunction perovskite solar cells by vapour deposition. *Nature* **501**, 395–398 (2013).
33. W. S. Yang, N. J. Noh, N. J. Jeon, Y. C. Kim, S. Ryu, J. W. Seo, S. I. Seok, High-performance photovoltaic perovskite layers fabricated through intramolecular exchange. *Science* **348**, 1234–1237 (2015).
34. M. Kuang, L. Wang, Y. Song, Controllable printing droplets for high-resolution patterns. *Adv. Mater.* **26**, 6950–6958 (2014).
35. D. Ge, L. Yang, G. Wu, S. Yang, Spray coating of superhydrophobic and angle-independent coloured films. *Chem. Commun.* **50**, 2469–2472 (2014).
36. A.-L. Barabási, H. E. Stanley, *Fractal Concepts in Surface Growth* (Cambridge Univ. Press, 1995).
37. L. Gao, W. Ren, H. Xu, L. Jin, Z. Wang, T. Ma, L.-P. Ma, Z. Zhang, Q. Fu, L.-M. Peng, X. Bao, H.-M. Cheng, Repeated growth and bubbling transfer of graphene with millimetre-size single-crystal grains using platinum. *Nat. Commun.* **3**, 699 (2012).
38. Y.-H. Lee, X.-Q. Zhang, W. Zhang, M.-T. Chang, C.-T. Lin, K.-D. Chang, Y.-C. Yu, J. T.-W. Wang, C.-S. Chang, L.-J. Li, T.-W. Lin, Synthesis of large-area MoS_2 atomic layers with chemical vapor deposition. *Adv. Mater.* **24**, 2320–2325 (2012).
39. W. Deng, X. Zhang, L. Huang, X. Xu, L. Wang, J. Wang, Q. Shang, S.-T. Lee, J. Jie, Aligned single-crystalline perovskite microwire arrays for high-performance flexible image sensors with long-term stability. *Adv. Mater.* **28**, 2201–2208 (2016).

Acknowledgments

Funding: Y.S. is grateful for the financial support of the National Key R&D Program of China (grants 2018YFA0208501, 2016YFB0401603, 2016YFC1100502, and 2016YFB0401100); the National Nature Science Foundation (grants 21522308, 51573192, 51773206, and 51473173); External Cooperation Program of Bureau of International Cooperation, Chinese Academy of Sciences (grant 121111KYSB20150022); and the "Strategic Priority Research Program" of Chinese Academy of Sciences (grant XDA09020000). **Author contributions:** Y.S. conceived and designed experiments. Z.G. performed experiments, data collection, and analysis. Z.H. assisted in crystallization model analysis. C.L. assisted in the device performance measurement. Z.G., M.L., and Y.S. wrote the manuscript. All authors discussed and commented on the manuscript. **Competing interests:** The authors declare that they have no competing interests. **Date and materials availability:** All data needed to evaluate the conclusions in the paper are present in the paper and/or the Supplementary Materials. Additional data related to this paper may be requested from the authors.

Submitted 7 February 2018
Accepted 17 May 2018
Published 29 June 2018
10.1126/sciadv.aat2390

Citation: Z. Gu, Z. Huang, C. Li, M. Li, Y. Song, A general printing approach for scalable growth of perovskite single-crystal films. *Sci. Adv.* **4**, eaat2390 (2018).

Science Advances

A general printing approach for scalable growth of perovskite single-crystal films

Zhenkun Gu, Zhandong Huang, Chang Li, Mingzhu Li and Yanlin Song

Sci Adv **4** (6), eaat2390.
DOI: 10.1126/sciadv.aat2390